nature energy

Article

https://doi.org/10.1038/s41560-026-02018-5

Alkali-metal-mediated control of phase segregation for flexible kesterite solar cells and modules with improved efficiency

Received: 8 February 2025

Accepted: 27 February 2026

Published online: 20 March 2026

Check for updates

Xiao Xu[1,2,7], Jinlin Wang[1,7], Menghan Jiao[1,3], Bowen Zhang[1,3], Tan Guo[1,4], Yuan Li[1], Jingchen Wang[1,3], Shudan Chen[1,3], Yiming Li[1], Dongmei Li[1,3,5], Jiangjian Shi[1] ✉, Huijue Wu[1], Wensheng Yan[2] ✉, Yanhong Luo[1,3,5] & Qingbo Meng[1,5,6] ✉

Flexible kesterite $Cu_2ZnSn(S,Se)_4$ (CZTSSe) photovoltaics are attractive for lightweight and portable applications, but their efficiency remains limited by uncontrolled alkali-metal incorporation. Here we elucidate and exploit the distinct and complementary roles of Na and Li in controlling CZTSSe crystallization on flexible substrates. Our results show that Na promotes crystal growth, but its induced Se enrichment simultaneously drives large-scale $SnSe_x$ phase segregation. The incorporation of Li reshapes the free-energy landscape of Cu-related phases, promoting the formation of Cu_xSe that consumes Se and thereby suppressing $SnSe_x$ phase growth while driving ordered phase evolution. This kinetic competition strategy yields high-quality CZTSSe films with reduced charge recombination loss and enables power conversion efficiencies of 14.5% (certified 14.2%) for flexible cells and 12.7% (certified 12.0%) for shingled modules. Our results provide mechanistic insights into alkali-metal regulation in chalcogenide solar cells and demonstrate a kinetic competition strategy that can be generalized to regulate crystallization in complex multinary materials.

Kesterite CZTSSe is an attractive thin-film photovoltaic material due to its abundance, non-toxicity and low-cost elemental composition[1,2]. Its low weight and mechanical flexibility further open opportunities for integrable photovoltaics and portable electronics[3]. Realizing these applications, however, requires the development of efficient CZTSSe solar cells and modules on flexible substrates such as metal foils or polymer films. Despite intensive research, the performance of flexible CZTSSe devices still lags markedly behind that of rigid counterparts[4–6], and module demonstration has not yet been achieved.

A major bottleneck in flexible devices is the lack of stable and controllable alkali-metal incorporation from substrates[7]. Drawing on the strategies developed since the copper–indium–gallium–selenide (CIGS) era, similar alkali-metal approaches have been applied to flexible CZTSSe cells to relieve this issue, obtaining notable efficiency gains[8–10]. Yet, these efforts remain insufficient to close the significant ~3% efficiency gap with rigid devices[4–6]. Moreover, owing to disparate experimental routes across studies, the reported roles of alkali metals remain ambiguous and often contentious. For instance, the frequently

[1]Beijing National Laboratory for Condensed Matter Physics, Institute of Physics, Chinese Academy of Sciences, Beijing, P. R. China. [2]Institute of Carbon Neutrality and New Energy, School of Electronics and Information, Hangzhou Dianzi University, Hangzhou, P. R. China. [3]School of Physical Sciences, University of Chinese Academy of Sciences, Beijing, P. R. China. [4]College of Materials Sciences and Opto-Electronic Technology, University of Chinese Academy of Sciences, Beijing, P. R. China. [5]Songshan Lake Materials Laboratory, Dongguan, P. R. China. [6]Center of Materials Science and Optoelectronics Engineering, University of Chinese Academy of Sciences, Beijing, P. R. China. [7]These authors contributed equally: Xiao Xu, Jinlin Wang. ✉e-mail: shijj@iphy.ac.cn; wensheng.yan@hdu.edu.cn; qbmeng@iphy.ac.cn

mentioned liquid-phase mechanism of Na_2Se appears inconsistent with its high melting point[11,12], and the mechanistic role of Li in chalcogenide absorbers is still unclear—with divergent interpretations ranging from substitutional doping to liquid-phase-assisted growth and to band-structure modulation[13–16]. These uncertainties, amplified by the significant complexity in composition and phase of CZTSSe, highlight the challenge of empirically introducing alkali metals to control CZTSSe crystallization, particularly involving complex phase-evolution and mass-transport processes, and thus underscores the critical necessity of establishing a more comprehensive and mechanistically grounded understanding of alkali-metal roles in these material systems.

Here we systematically reveal how alkali metals govern CZTSSe crystallization and phase evolution on flexible Mo foils. It is found that Na enriches Se in the system, promoting crystal growth but simultaneously driving uncontrolled $SnSe_x$ formation and micrometre-scale segregation. Complementarily, introducing Li reshapes the free-energy landscape, facilitating Cu-rich phase growth. By competitively consuming Se, this suppresses large-scale $SnSe_x$ segregation and its induced Cu–Sn separation, thereby mitigating the adverse effects associated with Na and enabling the orderly evolution of Cu_2SnSe_3 and CZTSSe. Leveraging this complementary interplay between Na and Li, we achieve high-quality CZTSSe films with a flexible device efficiency of 14.5% (certified 14.2%). CZTSSe-shingled modules were also constructed, achieving a power conversion efficiency (PCE) of 12.7% (certified 12.0%) over 10 cm^2. This value surpasses the long-standing 11.8% efficiency (uncertified) set a decade ago on vacuum-based rigid modules, thereby marking a demonstration where flexible modules outperform their rigid counterparts. Overall, this work clarifies the distinct and complementary roles of Na and Li and highlights the importance of phase-segregation-scale control in CZTSSe crystallization growth. More broadly, the kinetic competition strategy demonstrated here offers a generalizable framework for regulating multiphase evolution in complex material systems.

The beneficial and adverse roles of Na

As an initial step, we employed a widely used strategy to introduce Na into the system by directly dissolving NaCl into the precursor solution. The final CZTSSe layers were obtained by selenization of precursor films (Supplementary Fig. 1). As shown in Fig. 1a, the introduction of Na significantly reduces voids and inhomogeneous morphology, particularly eliminating the poor-conductivity-induced bright-contrast regions in scanning electron microscopy (SEM) images[17], on the film surface and promoted growth of the underlying grains. These regions in the Na-free control samples with poor conductivity were revealed to have a correlation with Zn local enrichment, probably in the form of a Zn-rich secondary phase (Supplementary Figs. 2–5).

Correspondingly, the Na-doped cell exhibited significant efficiency improvements, as shown in Fig. 1b. Specifically, the average PCE increased from 7.64 to 12.13%, with the short-circuit current density (J_{SC}) rising from 31.99 to 35.10 mA cm^{-2} and the fill factor (FF) increasing from ~0.5 to ~0.7. The average open-circuit voltage (V_{OC}) showed only a modest change from ~485 to ~490 mV, primarily benefiting from an increase in the bandgap (by ~10 meV) of CZTSSe with a slightly higher S content[18] (Supplementary Figs. 6–8). Such a small increase in V_{OC} is in sharp contrast to the FF, indicating that the improvement in the cell performance is mainly due to the enhancement in the charge transport properties of the CZTSSe layer, primarily benefiting from the morphology improvements, while the defect properties have not been fundamentally improved. The obvious reduction in the series resistance and ideality factor shown in Fig. 1c agrees well with this result.

Generally, improvements in crystallographic morphology of CZTSSe films are accompanied by a reduction in defect density[19], which appears to contrast with our observations. This further highlights the discrepancies in both experimental observations and mechanistic understanding regarding the effect of the alkali metal Na on CZTSSe. To clarify this, we further investigated the impact of Na incorporation on CZTSSe crystallization. To capture and observe intermediate crystallization processes, we parepared a sample selenized at a low temperature (450 °C) for a short duration (300 s; Supplementary Fig. 1). This selenization condition (450 °C, 300 s) was used for all the intermediate-state film preparations unless otherwise stated. As in Fig. 1d, a pronounced non-CZTSSe Raman peak at ~250 cm^{-1} was observed in the Na-containing sample, which is typically attributed to the vibrational of elemental Se (ref. 20). This indicates that Na incorporation realizes the surface enrichment of elemental Se, which can perform as a liquid-phase medium to assist the CZTSSe crystal growth at elevated temperatures, thus explaining the observed enhancement in CZTSSe crystallinity. However, a marked enhancement of the Raman signal at ~116 cm^{-1} was also observed in the Na-containing sample, indicating the formation of a layered $SnSe_x$ phase[21]. Raman mapping of these films (Fig. 1e,f) further revealed large-scale distributions of $SnSe_x$ in the Na-containing sample, whereas such a phenomenon was absent in the control sample. Previous studies suggested that the formation of $SnSe_x$ during intermediate stages is detrimental to CZTSSe phase evolution and potentially introduces surface recombination[19,22]. This suggestion may explain why, despite the improved crystallinity in Na-containing CZTSSe, the V_{OC} of the cells did not show a concurrent improvement.

We further investigated the effect of Na on a simpler $Cu_2Sn(S,Se)_3$ (CTSSe) system, as it is a critical step in the phase evolution of CZTSSe. After a similar 450 °C and 300 s selenization, large Sn-rich regions were also observed in the SEM and energy-dispersive X-ray spectroscopy (EDX) images of the CTSSe film (Fig. 1g,h and Supplementary Fig. 9), forming a spatial distribution similar to that observed in CZTSSe via Raman mapping. Outside these Sn-rich domains, Cu enrichment was observed, forming significant Cu–Sn phase separation, with a characteristic length scale of ~10 µm. Such extensive phase separation is expected to significantly impede Cu–Sn interdiffusion during subsequent crystallization processing, thereby hindering the formation of CTSSe. In CZTSSe, however, blocking or slowing the phase evolution would inevitably induce defect formations.

The compensating role of Li

Figure 2a schematically illustrates the possible mechanism underlying the large-scale Cu–Sn phase separations observed in these films. First, Na incorporation markedly increases the surface Se content through Na–Se interactions[12], the detailed mechanism of which will be discussed elsewhere. The elevated Se content provides an enhanced driving force for the growth of all the metal selenides. This inevitably promotes the uncontrolled growth of $SnSe_x$, particularly because it has a much lower melting point[23,24], giving rise to the extensive planar structures observed experimentally. Although Cu_xSe and $SnSe_x$ are thermodynamically expected to merge into the Cu_2SnSe_3 phase[25], the sheet-like morphology of $SnSe_x$ restricts intimate contact with Cu_xSe, thereby limiting elemental interdiffusion and phase transformation. This suggests that accelerating the fusion of these phases requires suppressing the rapid growth of $SnSe_x$ sheets and reducing their lateral dimensions to enhance contact with Cu_xSe. However, achieving this appears to be a considerable challenge under the Na-induced Se-rich environment.

Considering the situation from a kinetic perspective, the growth of different phases within the film inherently competes for Se consumption. In other words, accelerating the formation of the Cu_xSe phase and its uptake of Se would correspondingly suppress the growth of $SnSe_x$, thereby reducing the lateral dimensions of the $SnSe_x$ sheets. First-principles calculations (Fig. 2b, Supplementary Fig. 10 and Supplementary Table 1) revealed that Li incorporation can effectively lower the Gibbs free energies of both Cu_2Se and Cu_2SnSe_3, granting them a greater growth advantage during high-temperature selenization (Fig. 2c).

Guided by this theoretical prediction, we introduced Li into the CZTSSe film preparation to relieve the adverse effects caused by Na.

https://doi.org/10.1038/s41560-026-02018-5

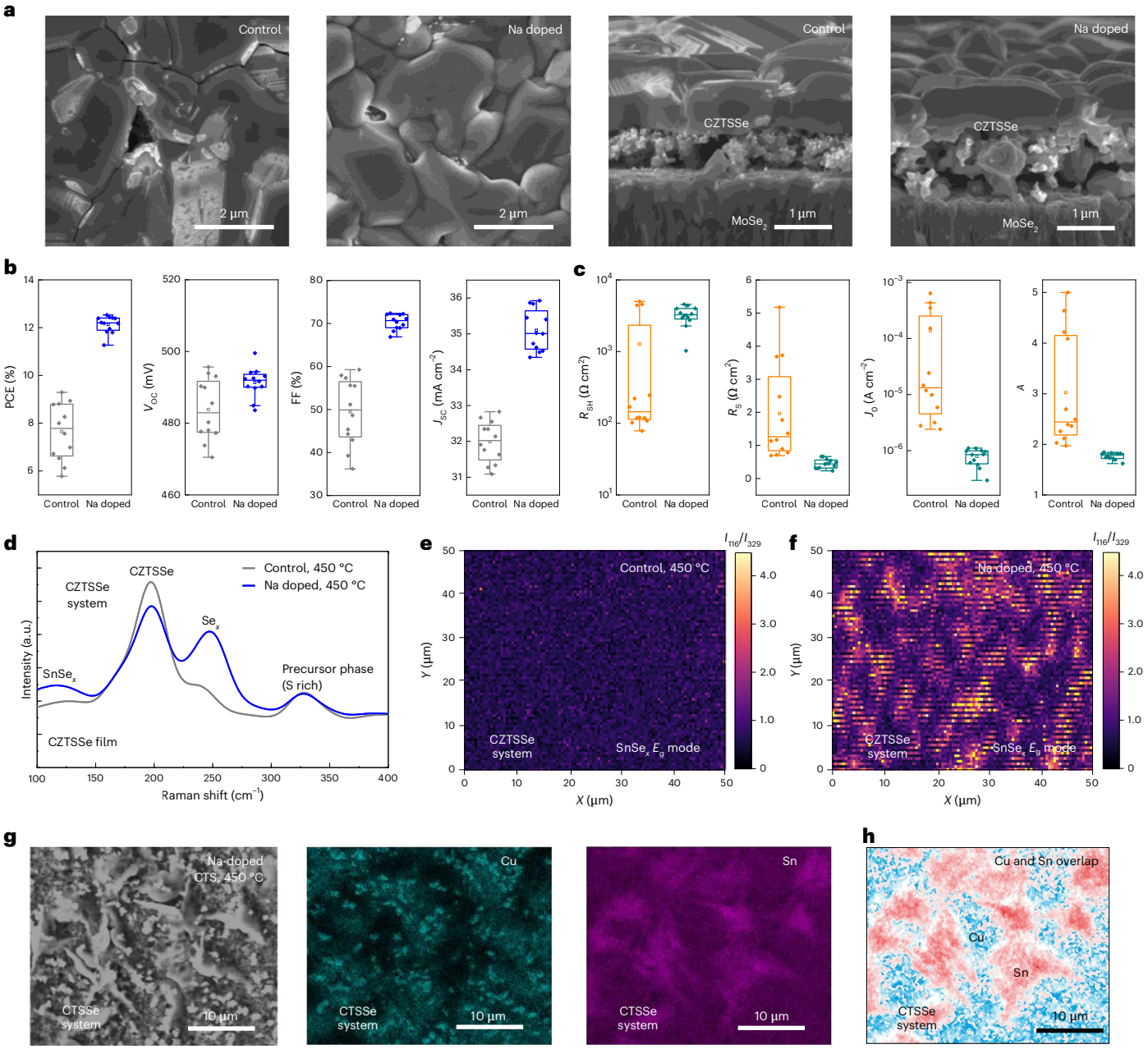

Fig. 1 | Effect of Na doping on film properties. a, Top-view and cross-sectional SEM images of control and Na-doped films. **b**,**c**, Statistics of device performance and heterojunction electric parameters of the cells. Centre line indicates the median; box limits represent the 25th and 75th percentiles; whiskers extend to ×1.5 the interquartile range; raw data points are shown. Each box contains 12 individual solar cells. R_{SH}, shunt resistance; R_S, series resistance; A, ideality factor. **d**–**f**, Raman spectra and mapping (intensity ratio between 116 and 329 cm^{-1} peaks (I_{116}/I_{329}) corresponding to ration between $SnSe_x$ and precursor phase, respectively) of the control and Na-doped CZTSSe films selenized at 450 °C for 300 s. **g**, Top-view SEM image and Cu and Sn EDX element distributions of the Na-doped $Cu_2Sn(S,Se)_3$ (CTSSe) film (selenized at 450 °C for 300 s). **h**, The overlap of the Cu (blue colour) and Sn (red colour) elemental distributions.

In the experiment, we first optimized the approach for the Li introduction. As an initial attempt, LiCl was added into a Na-containing precursor solution to form a uniform Na–Li co-doped precursor solution. Thin films were then prepared using multilayer coating processes (Supplementary Fig. 11). We found that, although a small amount of Li incorporation obviously enhanced the V_{OC} and efficiency of the cells, the FF showed a noticeable decline (Supplementary Fig. 12). This result aligns with previous literature results and our own experiments[26], where simple Li-doped CZTSSe devices often exhibited a relatively low FF. To investigate further, the vertical elemental distribution in the precursor films was measured (Supplementary Fig. 13). A very high concentration of Li was found at the film surface, likely due to the re-dissolution phenomenon during multiple coating steps[13]. This may be detrimental to the cell performance. However, simply reducing the concentration of Li in the precursor solution cannot overcome this issue (Supplementary Fig. 12). To address this, we developed a non-uniform Li introduction strategy (Supplementary Fig. 11). Specifically, the Li-containing solution was used only for coating the first precursor layer on the Mo substrate, with the subsequent layers coated using a solution containing only Na. This approach can suppress the re-dissolution of Li in the lower layers, thus reducing surface Li accumulation without significantly affecting the bulk Li content (Supplementary Fig. 13). Using this method, a further improved FF was observed in the cells while maintaining both J_{SC} and

https://doi.org/10.1038/s41560-026-02018-5

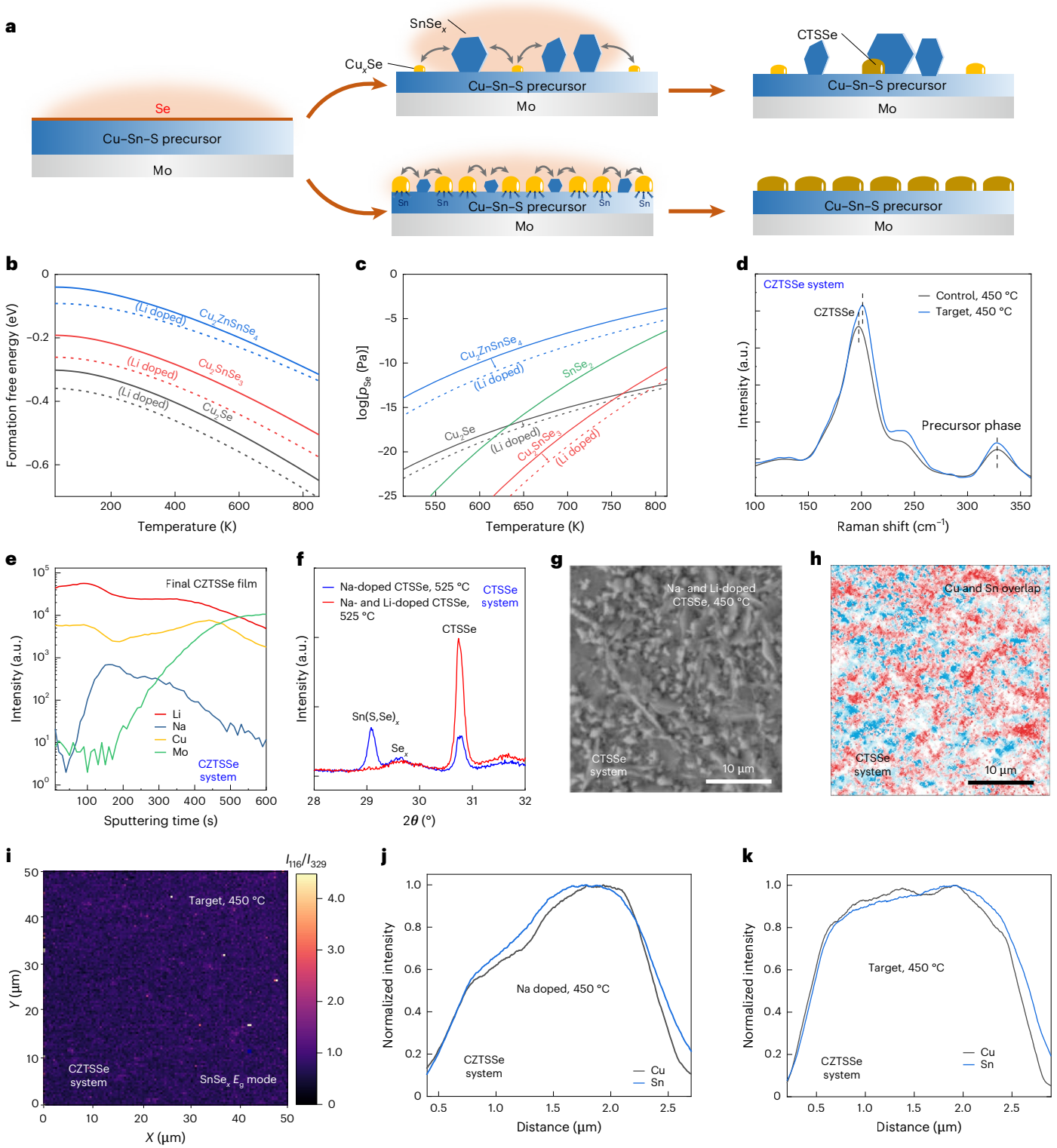

Fig. 2 | Effect of further Li incorporation on phase separation. a, Schematic diagram of the Cu–Sn phase separations observed in the films. **b**,**c**, Effect of Li incorporation on the Gibbs free energies and formation characteristics (selenium vapour pressure p_{Se} versus temperature) of Cu_2Se, Cu_2SnSe_3 and $Cu_2ZnSnSe_4$ (ref. 39). **d**, Raman spectra of the control CZTSSe film and that with both Na and Li doping (selenized at 450 °C for 300 s). The target sample corresponds to an optimal non-uniform Na–Li incorporation strategy (Supplementary Fig. 13). **e**, Secondary ion mass spectrometry elemental profiling of the final-state selenized target CZTSSe film. **f**, X-ray diffraction of Na-doped CTSSe films (selenized at 525 °C for 300 s) without or with further Li incorporation. 2θ, the angle between the transmitted beam and reflected beam. **g**,**h**, Top-view SEM image and Cu–Sn EDX mapping overlaps of these CTSSe films. Colour in **h**: Sn, red; Cu, blue. **i**, Raman mapping (intensity ratio between 116 and 329 cm^{-1} peaks) of the target CZTSSe film (selenized at 450 °C for 300 s). **j**,**k**, Cross-sectional EDX profiles of Cu and Sn in Na-doped (**j**) and target (**k**) CZTSSe films (selenized at 450 °C for 300 s).

V_{OC} (Supplementary Figs. 14 and 15). This result demonstrates that we can leverage the beneficial effects of Li while minimizing the negative consequences of its local accumulation. For clarity, in the following, the sample based on the optimal Na–Li condition will be denoted as the target sample (details are in the Methods).

Based on this, we turned our focus to investigating the impact of further Li incorporation on the microscopic-scale characteristics of phase evolution in CZTSSe films. First, Raman spectra of the intermediate target sample showed a slight blueshift after the Li incorporation (Fig. 2d). After excluding the possible influence of variations in S content (Supplementary Fig. 16), the observed Raman peak shift suggests that Li had incorporated into the lattice, providing a structural basis for its regulation of phase evolution in this system. Secondary ion mass spectrometry (Fig. 2e) also showed Li distribution closely correlated with Cu in the top layers of the final-state CZTSSe films, providing further evidence of its involvement in crystal growth. By contrast, Na is found at much lower relative concentrations in the large-grained upper layers of the final films, again highlighting the distinct roles by which Li and Na affect CZTSSe crystallization.

The effect of the Li incorporation on the growth of Sn-related and Cu-related phases is clearly manifested in the CTSSe film system. X-ray diffraction analysis showed that further Li incorporation enhanced the Cu_x(S,Se) peak at 450 °C and the CTSSe peak at 525 °C (Fig. 2f and Supplementary Fig. 17), accompanied by a significant suppression of $SnSe_x$. These results indicate that Li accelerates the conversion of Cu and Sn into the desired CTSSe phase. SEM images of the CTSSe film further reveal a significant reduction in the phase separation when compared with that of the Na-doped sample, as already shown in Fig. 1g,h: large plate domains vanish, giving way to more granular Cu-rich grains between which Sn is more uniformly dispersed (Fig. 2g,h and Supplementary Fig. 18). The distributions of the Cu and Sn elements were fully interspersed, with the phase separation scale reducing to ~1 µm or smaller. In the target CZTSSe sample (Fig. 2i; 450 °C, 300 s), the $SnSe_x$ phase was also no longer observed via Raman mapping. Clearly, this reduced phase separation can enhance the elemental interdiffusion, facilitating crystal growth and ultimately improving the quality of CZTSSe films by providing more-uniform vertical element distribution (Fig. 2j,k and Supplementary Figs. 19 and 20).

Solar cell performance and photoelectric characterization

We further evaluated the cell performance (Fig. 3 and Supplementary Fig. 14). In Fig. 3a, the effects of Na and Li concentrations on device efficiency in the non-uniform alkali-metal precursor-film strategy are first presented. With increasing Na concentration, the device efficiency shows an overall upward trend. Under the optimal Na concentration of 80 mM, further introducing 120 mM LiCl into the first layer of the precursor film leads to an additional absolute increase of approximately 2% in the average device efficiency. In particular, the average V_{OC} increased markedly from ~490 mV to ~530 mV, while the J_{SC} also showed a pronounced enhancement, reaching ~37 mA cm^{-2} (Fig. 3b). The V_{OC} increase is obviously higher than the bandgap change (Supplementary Fig. 6), and the reverse saturation current density (J_0) also exhibited a substantial reduction under a similar ideality factor (Supplementary Fig. 21), clearly indicating a suppression of non-radiative charge losses.

Ultimately, we realized a total-area efficiency of 14.45% in the cell, with a J_{SC} of 36.8 mA cm^{-2}, V_{OC} of 540.4 mV and FF of ~0.73 (Fig. 3c). The exceptionally high FF demonstrates the significant improvements in charge transport and the mitigation of charge recombination loss of the cell, which also translated into a high external quantum efficiency (EQE) across a broad spectral range. The EQE spectrum (Fig. 3d) gives an active-area J_{SC} integration of 38.67 mA cm^{-2} and suggests a bandgap of ~1.08 eV for the CZTSSe absorber. By benchmarking against the theoretical limit, we further analysed the performance parameters of the cells (Fig. 3e). Specifically, the V_{OC} × FF value of our devices reached 54% of its theoretical limit, while the J_{SC} attained 83%, representing a significant improvement compared with previous results. Nevertheless, similar to rigid counterparts, suppressing non-radiative charge recombination remains crucial for further efficiency enhancement of these cells.

One of our cells was also certified in an accredited third-party lab (National Photovoltaic Industry Measurement and Testing Center, NPVM), yielding a total-area efficiency of ~14.2% (Supplementary Fig. 22). Beyond efficiency, we also measured the mechanical bending stability of these devices. The target cell exhibited the best mechanical reliability, with its efficiency degraded by only ~2% when it was bent at a radius of 8 mm (Supplementary Figs. 23 and 24). After 1,000 cycles of bending at a 20 mm radius, the cell showed almost no performance degradation. By contrast, ~5% and ~25% efficiency degradations were observed in the Na-doped cell and control cell, respectively. Such remarkable improvements in both device efficiency and mechanical bending stability provide an essential foundation for future applications.

To further understand the physical mechanism of the effects of Na and Li, defects and optoelectronic properties of CZTSSe films and devices were also investigated. Photoluminescence (PL) measurements (Fig. 4a,b) revealed that Na incorporation moderately enhanced the luminescence of CZTSSe films while having only a little influence on the PL peak position, by ~10 meV, corresponding to the bandgap change. This further confirmed that although Na improved the microstructural morphology of the films through the introduction of excess Se, its effect on defect states and band-tail distributions in CZTSSe was limited. By contrast, further Li incorporation induced a pronounced blueshift of the PL peak by ~100 meV, accompanied by a further increase in PL intensity. Temperature-dependent PL measurements confirmed both the intensity enhancement and the peak blueshift. Particularly, modelling of the relationship between the intensity and peak energy of PL indicates that the target sample possessed the smallest luminescence redshift relative to its bandgap (Supplementary Fig. 6),and the narrowest distribution and the lowest density of states of band-tail states, whereas the Na-doped and control samples exhibited similar luminescence redshifts and state distribution-width parameters (Supplementary Note 2, Supplementary Fig. 25 and Supplementary Table 3). This result clearly suggests that further Li incorporation significantly suppresses the deep defect-induced potential fluctuations in CZTSSe[27].

Thermal admittance spectroscopy was also measured to assess defect properties. It was found that Cu_{Zn} defects dominated the capacitance response across all three samples (Fig. 4c), while the target one exhibited a moderate reduction in defect density and a shallowing of defect ionization energy by ~30 meV (ref. 28). Moreover, the target sample displayed a pronounced decrease in the capture cross-section, from 10^{-16} to 10^{-17} cm^2, whereas the Na-doped device showed only a 1/2 reduction to that of the control sample (Fig. 4d). This substantial decrease in the charge-trapping cross-section reflects a significant improvement in lattice ordering and a reduction in structural distortion, fully consistent with the observed PL blueshift in the target CZTSSe films. Such improvements would diminish the trapping activity of deep defects, thus contributing to the pronounced enhancement in V_{OC} (ref. 29).

The spatial distribution of the defect charge was probed using capacitance–voltage (C–V) and driving-level capacitance profiling (DLCP) methods. These methods revealed that the interfacial defect density in the cell was markedly reduced upon the synergistic incorporation of Na and Li, from ~7×10^{15} cm^{-3} in the control devices to ~2×10^{15} cm^{-3} (ref. 30; Fig. 4e). This reduction is likely attributed to the improved film morphology and the elimination of Sn-rich surface phases. For the free-carrier distribution extracted from high-frequency DLCP (Fig. 4f), we found that both Na and Li can enhance interfacial-carrier concentration while reducing bulk carrier concentration, with the effect being most pronounced in the target sample. In CZTSSe, the improved crystallization and reduced

https://doi.org/10.1038/s41560-026-02018-5

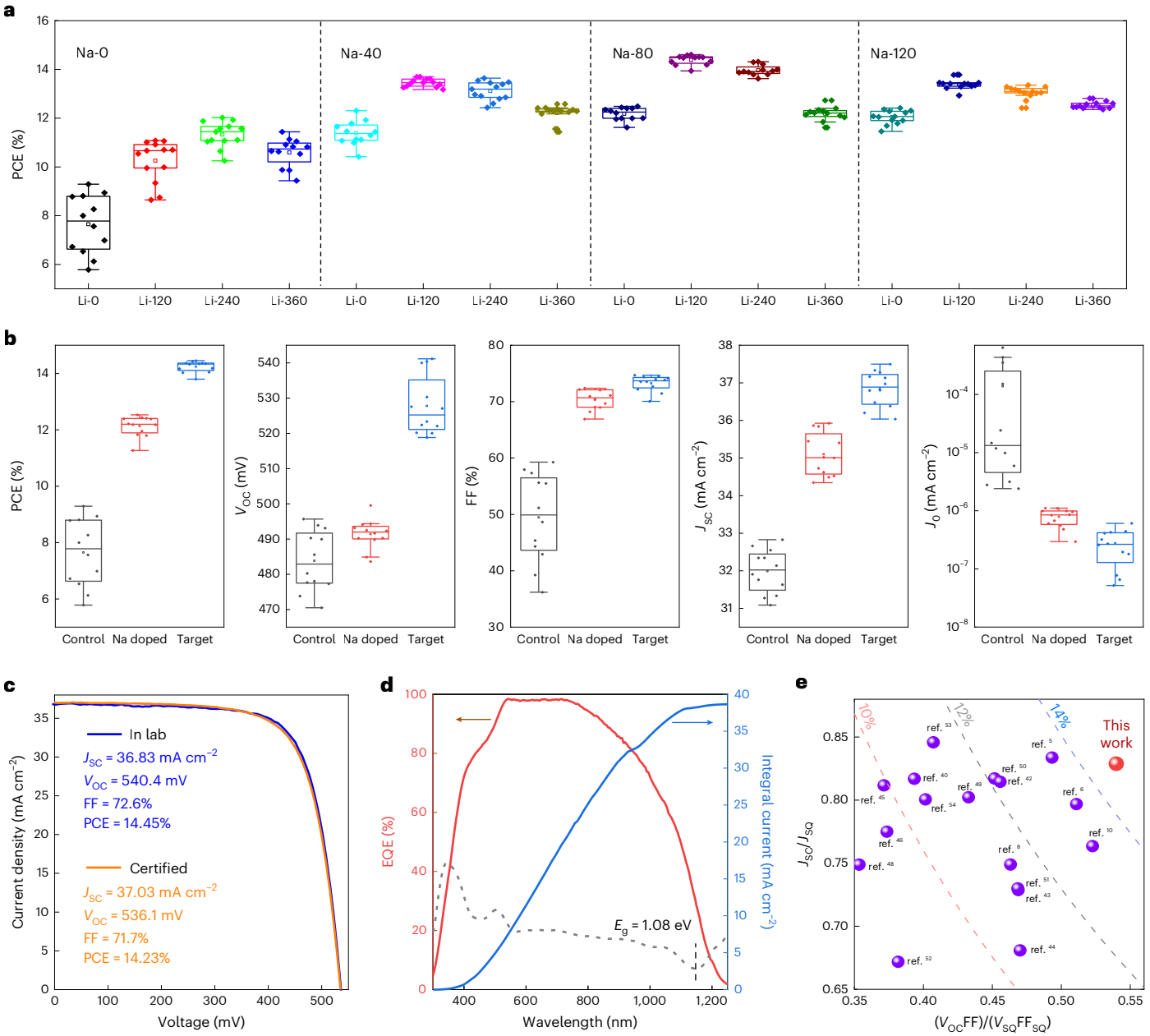

Fig. 3 | Device performance. a, Statistics of performance parameters of the cells based on different Na and Li incorporation concentrations in a non-uniform strategy (Supplementary Fig. 7). For clarity, the sample is denoted as Na-*X* and Li-*X*, where *X* corresponds to the alkali-metal concentration (in units of millimolar, mM) in the corresponding precursor solutions. Centre line indicates the median; box limits represent the 25th and 75th percentiles; whiskers extend to ×1.5 the interquartile range; raw data points are shown. Each box contains 12 individual solar cells. **b**, Statistics of device performance parameters for control, Na-doped and target cells. Centre line indicates the median; box limits represent the 25th and 75th percentiles; whiskers extend to ×1.5 the interquartile range; raw data points are shown. Each box contains 12 individual solar cells. **c**, Current density–voltage (*J*–*V*) curve of the champion flexible CZTSSe solar cell on Mo foil substrates measured in our lab and certified at NPVM. **d**, EQE spectrum and the corresponding integrated current density of the cell, with the dEQE/dλ curve for bandgap estimation (λ, wavelength; vertical dashed line depicts the bandgap position). **e**, Comparison of performance parameters of flexible CZTSSe devices reported in recent years (detailed in Supplementary Table 2) to the Shockley-Queisser (SQ) theoretical limit[5,6,8,10,40–54].

lattice distortion are usually accompanied by the decrease in Cu_{Zn} self-doping[31], which may lead to the reduction in bulk carrier concentration, while for the enhanced surface-carrier concentration, it may result from a reduction in the surface donor defects, such as S or Se vacancies[32], or to increased Cu vacancies induced by Na or Li (ref. 33). From a heterojunction perspective, the increased interfacial-carrier density enables a stronger interface electric field and energy-band bending[34], facilitating charge extraction and more effectively suppressing charge recombination. This effect on charge recombination was clearly demonstrated by the photovoltage decay of the cells biased at 300 mV, where a significantly prolonged photovoltage lifetime was observed in the target sample (Fig. 4g). Meanwhile, the Na-doped cell exhibited the fastest photovoltage decay, which may arise from a more severe surface recombination due to $SnSe_x$ intermediate phases or from an improved charge transport compared with the control one.

The improvements in charge transport in the Na-doped and target samples were indeed observed by using modulated transient photocurrent (m-TPC) measurements (Fig. 4h–j). Both of these two samples exhibited sharper m-TPC peaks and faster decay compared

https://doi.org/10.1038/s41560-026-02018-5

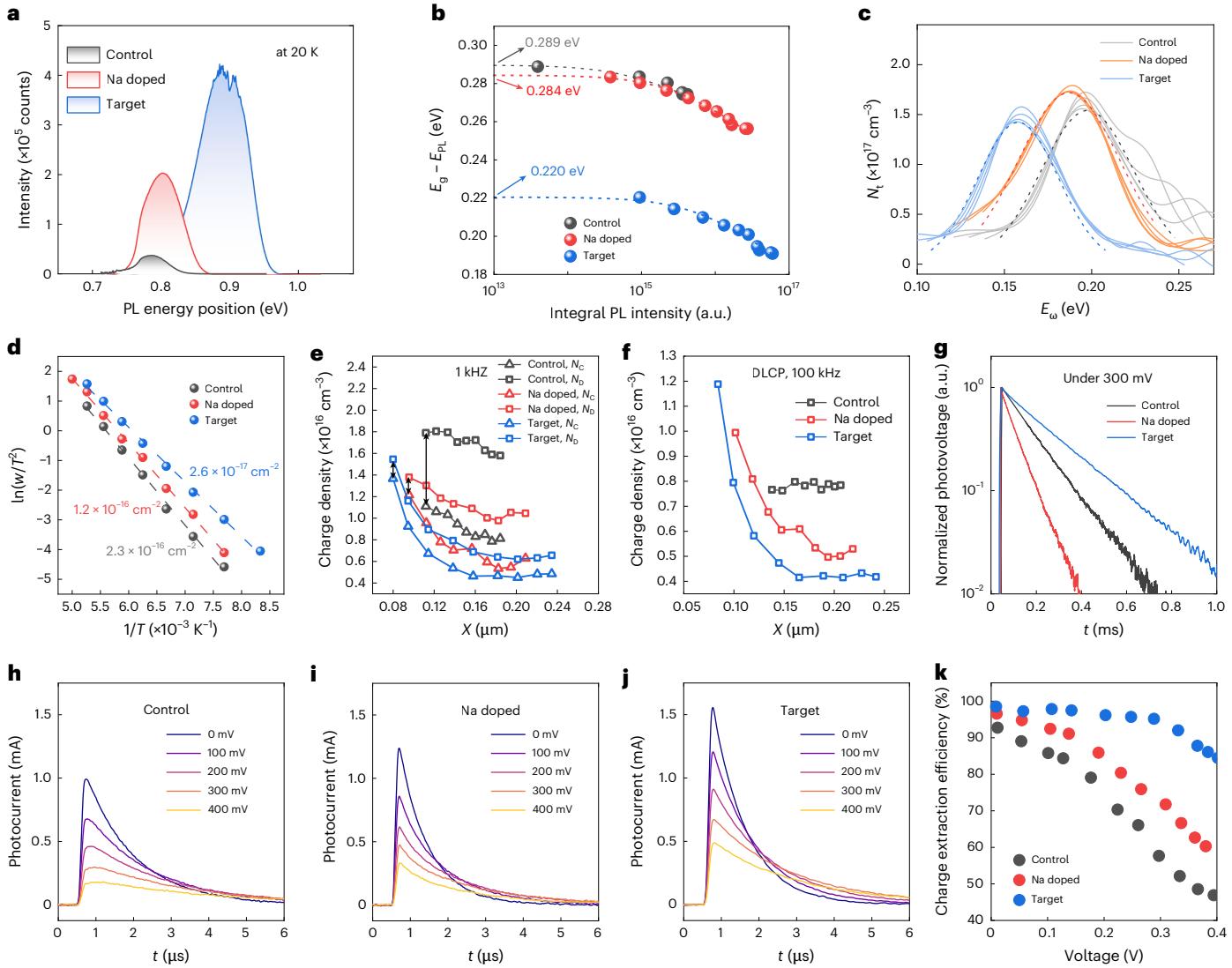

Fig. 4 | Defect properties and carrier-transport characteristics. a, PL spectra of control, Na-doped and target CZTSSe films at 20 K. **b**, The correlation between PL peak energy (relative to bandgaps, $E_g - E_{PL}$. E_{PL}, measured PL peak energy) and PL intensity. The model of exponential distributed band-tail states is used for fitting (dashed lines; Supplementary Note 2). **c**, Energy-dependent defect distributions (N_t) obtained by thermal admittance spectroscopy, E_ω, where ω means the energy is derived from angular frequency. Dashed curves show Gaussian fits. **d**, Arrhenius plots from thermal admittance spectroscopy. Dashed lines indicate Arrhenius fits to extract carrier-capture cross-sections. **e**, *C*–*V* and DLCP of these samples. The difference in the charge density measured by *C*–*V* (N_C) and DLCP (N_D) reflects the interface defect density. **f**, Free-carrier distributions of these samples measured by DLCP at high frequency. **g**, Photovoltage decay of these cells at 300 mV bias. *t*, time. **h**–**j**, Photocurrent decays of these cells under different bias voltages. **k**, Charge extraction efficiency of these cells derived from modulated electrical transient measurements.

with the control device, while the target cell further displayed a better charge retention ability under bias voltages, implying less charge loss. Quantitative analysis of the electrical transient characteristics (Fig. 4k and Supplementary Fig. 26) unambiguously confirmed a substantial enhancement of the charge extraction efficiency in the target device, further evidencing the reduced bulk-recombination losses in CZTSSe[35,36]. By contrast, Na incorporation led to limited improvements in charge extraction efficiency, as significant charge recombination remained within the CZTSSe films.

Briefly, these characterizations collectively support that Na incorporation primarily enhances charge transport of the CZTSSe films by improving the microstructural morphology, probably through liquid-selenium-assisted crystal growth. By contrast, the subsequent incorporation of Li further modulates the phase structure and its evolution at the microscopic scale, particularly mitigating the uncontrolled phase growth induced by Na. These compensatory effects ultimately enable a synergistic improvement in both charge transport and defective suppression of CZTSSe films, which underpins the remarkable performance enhancement of the flexible solar cells.

Demonstration of CZTSSe-shingled modules

Based on the high-performance flexible CZTSSe cells fabricated on conductive Mo foils, we further constructed shingled modules[37]. The structure of the shingled module is schematically illustrated in Fig. 5a, and the detailed fabrication process is shown in Supplementary Fig. 27. Specifically, flexible cells with a size of ~3.7 × 1.3 cm^2 were first prepared (Fig. 5b), in which fine grid electrodes were thermally evaporated onto the surface, and busbars were deposited along the edges. The back edge of the Mo foil substrate was then connected to the front busbar of another sub-cell using conductive silver paste, forming a series connection between the sub-cells. By interconnecting four sub-cells, we constructed a shingled module with an aperture area of >10.5 cm^2. To ensure robust interconnection, the module was further laminated and encapsulated with ethylene vinyl acetate (EVA) and polyethylene

https://doi.org/10.1038/s41560-026-02018-5

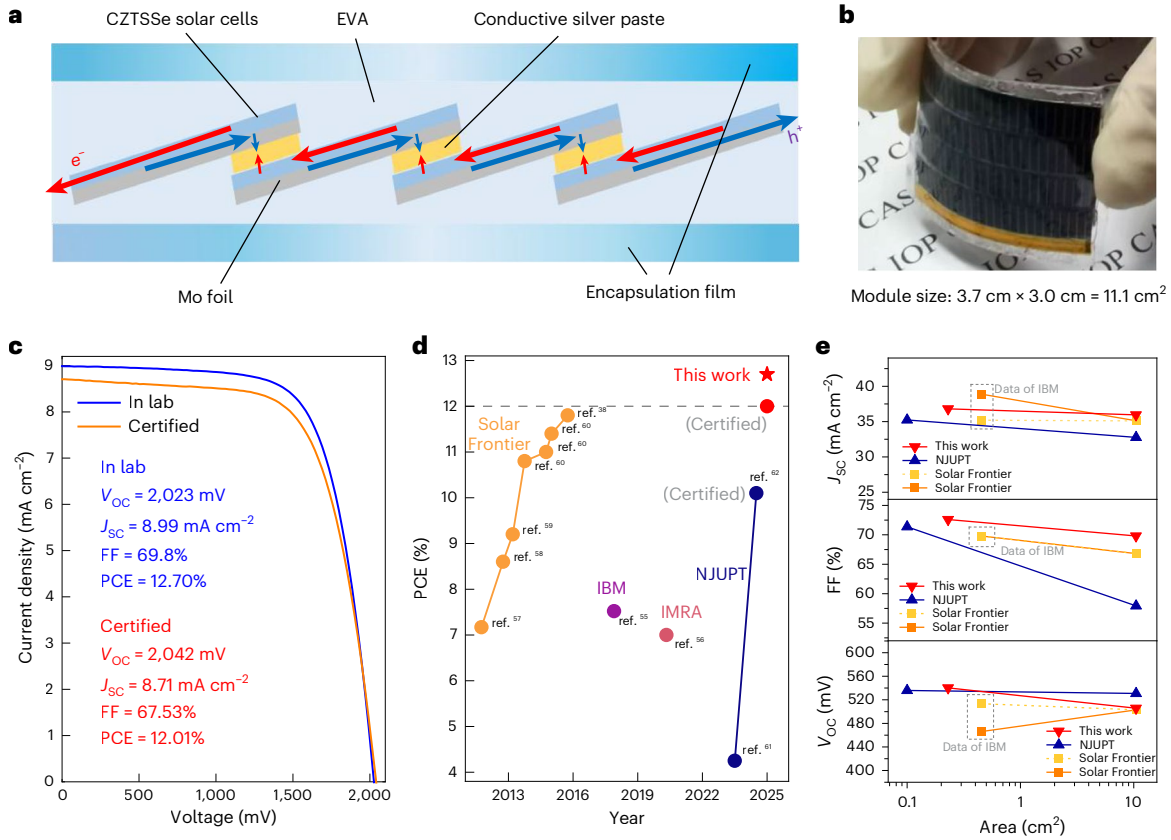

Fig. 5 | CZTSSe-shingled modules. a, Schematic diagram of the construction of a shingled module based on strip-shaped flexible CZTSSe cells. **b**, Photograph of a complete module. **c**, *J*–*V* curve of the champion module measured in our lab and corresponding certification result. **d**, Efficiency progress of CZTSSe photovoltaic modules over the past years[38,55–62]. IBM, International Business Machines Corporation; IMRA, Institut Minoru de Recherche Avancé; NJUPT, Nanjing University of Posts and Telecommunications. **e**, Analysis of the variation of device parameters from small-area cells to modules[38,62–64].

terephthalate (PET) films. In our laboratory measurements, the shingled module achieved a total-area efficiency of 12.7% (10.5 cm^2 mask), with a J_{SC} of ~9 mA cm^{-2}, V_{OC} of ~2.02 V and FF of ~70% (Fig. 5c).

The certification of the module by NPVM yielded an efficiency of ~12.0% (Supplementary Fig. 28), with a J_{SC} of ~8.7 mA cm^{-2} and FF of ~0.68. This performance markedly surpasses that of previously reported CZTSSe modules also fabricated via solution processing. This result also represents a breakthrough in CZTSSe modules since the 11.8% efficiency reported by Solar Frontier in 2015[38] (Fig. 5d), marking nearly a decade of progress, and also demonstrates that flexible modules have surpassed their rigid counterparts. This supports the feasibility of achieving high-performance CZTSSe modules through more diverse technological routes and thus laying the foundation for their further development and deployment across multiple application scenarios. The high storage and operational stabilities of our modules further strengthen their application potential (Supplementary Fig. 29). Shingled modules also exhibit a pronounced advantage in maintaining J_{SC} when scaled from small-area cells to large-area modules, reaching nearly 98% in our case (Fig. 5e). By contrast, for rigid modules fabricated via laser scribing, optical dead-zone losses of ~5% or even higher are invariably inevitable. This result also explains why shingling technology has recently been increasingly adopted in crystalline silicon solar cells. Nevertheless, similar to crystalline silicon solar cells, CZTSSe-shingled modules also face the issue of charge recombination at the sub-cell edges. This issue calls for further investigation, and its improvement will help achieve a higher retention of V_{OC} and FF at the module level.

Conclusion

In summary, to address the critical challenge of deliberately controlling alkali-metal incorporation in flexible CZTSSe solar cells, we systematically investigated the mechanistic roles of the alkali metals Na and Li. We found that Na incorporation improves CZTSSe crystallization and microstructural morphology, thereby boosting charge transport. However, the Na-induced excessive Se in the intermediate process simultaneously causes uncontrolled $SnSe_x$ phase growth and large-scale phase segregation. To overcome this issue, we proposed a kinetic competition strategy involving Se consumption to balance the growth of Cu_xSe and $SnSe_x$. We demonstrated that Li incorporation can achieve this balance by altering the free-energy landscape and formation characteristics of Cu-related phases, thereby effectively suppressing defects and non-radiative charge-recombination losses in CZTSSe. Harnessing the synergistic and compensatory effects of Na and Li, we achieved efficiencies of 14.45% (certified 14.2%) in flexible CZTSSe cells and 12.7% (certified 12.0%) in large-area shingled modules—marking a breakthrough in CZTSSe module performance since Solar Frontier's 11.8% efficiency, reported a decade ago, and notably, the important instance of flexible modules outperforming their rigid counterparts. Overall, our work not only demonstrates the feasibility of diverse technological routes for advancing CZTSSe photovoltaics, but more importantly, also provides mechanistic insights into the long-debated role of alkali metals in this complex material system.

Methods

Reagents and materials

Thiourea (99%, Alfa), 2-methoxyethanol (MOE; 99.8%, Aladdin), AgCl (99.5%, Innochem), CuCl (99.99%, Alfa), $SnCl_4$ (99.998%, Macklin), $Zn(Ac)_2$ (99.99%, Aladdin), $CdCl_2$ (99.99%, Aladdin), LiCl (99.99%, Innochem), NaCl (99.8%, Innochem) and molybdenum foil (≥99.95%, 0.1 mm thick, Qinghe County Haoxuan Metal Materials) were obtained.

CZTSSe precursor film preparation

First, 7.311 g thiourea was added into vial 1 containing 15 ml MOE and stirred until dissolved. Then, 0.345 g AgCl and 2.16 g CuCl were successively added into vial 1 and stirred until completely dissolved. Second, 15 ml MOE was injected into vial 2, containing 3.963 g $SnCl_4$, while stirring. Third, 3.126 g $Zn(Ac)_2$ was added into the $SnCl_4$–MOE suspension until thoroughly dissolved. Fourth, we mixed the solutions in vial 2 and vial 1 and obtained a clear precursor solution. All of the above steps were performed in a glove box. The filtered precursor solution was spin-coated onto a pre-cleaned Mo substrate at 2,000 rpm for 30 s, followed by annealing on a hotplate at 280 °C for 2 min. This coating–annealing process was repeated four times. Then, precursor films were placed in a graphite box containing Se particles and selenized in a rapid-heating tube furnace. The detailed selenization condition was as follows: the temperature was raised to 535 °C within 1 min and maintained for 20 min. The whole selenization process was performed under 1 atm with a N_2 flow of 80 sccm. To capture and observe the intermediate crystallization processes, samples selenized at a low temperature (450 °C) for a short duration (300 s) were also prepared. This selenization condition (450 °C, 300 s) was used for all the intermediate-state film preparation unless otherwise stated.

Alkali-metal incorporation

Alkali metals were introduced by adding NaCl and LiCl into the above precursor solutions. For Na-only doping, the same Na concentration was used in the precursor solution for each deposited layer of the precursor film. The concentration of NaCl was systematically optimized, and the optimal value was determined to be 60 mM. For uniform Na and Li co-doping, LiCl was further added to the optimized Na-containing precursor solution, and its concentration was also optimized for each layer of the precursor film. The optimal LiCl concentration for uniform co-doping was found to be 20 mM. To address the issues associated with uniform Na–Li co-doping, we further developed a non-uniform doping strategy, as described in the main text. Specifically, LiCl was introduced only into the first layer of the precursor film, while the remaining layers were deposited using precursor solutions containing only Na. The concentrations of LiCl in the first layer and NaCl in the other three layers were separately optimized. The final optimized concentrations were 80 mM for NaCl and 120 mM for LiCl.

CZTSSe device fabrication

An ~20–30-nm-thick CdS buffer layer was deposited on the top of CZTSSe films by the chemical bath deposition method, followed by sputtering a 30 nm intrinsic ZnO (i-ZnO) layer and 200 nm indium tin oxide (ITO) layer. Some 50 nm nickel (Ni) and 2 µm aluminium (Al) were evaporated on the ITO layer. A 110 nm MgF_2 layer covered the whole device, serving as the anti-reflection coating. Finally, the total area of each cell is ~0.24 cm^2. The aperture mask's area is 0.2296 cm^2, which was measured by optical microscope.

Film characterization

Raman spectra were carried out on a Raman spectrometer (LabRAM HR Evolution, HORIBA) using 532 nm laser diode as the excitation source. The Raman mapping's step is 0.42 µm. SEM images were measured on a Hitachi S4800 SEM instrument using 10 kV power. Element maps were obtained by an energy-dispersive spectrometer (Oxford AZtec X-Max 50) using 20 kV power. Kelvin probe force microscopy images were obtained on an atomic force microscope (Multimode 9, Bruker). The X-ray photoelectron spectroscopy characterizations were performed on an X-ray photoelectron spectrometer (Thermo Fisher Scientific ESCALAB 250Xi). Steady-state PL spectra were obtained using a PL spectrometer (Edinburgh Instruments, FLS 900), excited with a picosecond-pulsed diode laser (Edinburgh Instruments, EPL-640) with a wavelength of 638.2 nm while cooling with liquid helium. Secondary ion mass spectrometry analysis was performed using a TOF-SIMS 5 instrument (Iontof) with an O_2 gun sputter source at 1 keV (for the precursor film) or 2 keV (for the selenized film).

Free-energy calculation

The Gibbs free energy, ΔG_f, was computed to evaluate the thermodynamic stability of the compound. The free energy per atom is calculated using the following equation:

$$\Delta G_f(T,p)_{\text{per atom}} = [G(\text{compound}) - \sum n_i G(\text{element}_i)]/N_{\text{total}}$$

where G(compound) is the Gibbs free energy of the compound; $G(\text{element}_i)$ is the Gibbs free energy per atom of element i in its standard reference phase; n_i is the number of atoms of element i in the simulated model's chemical formula; N_{total} is the total number of atoms in the simulated model of the compound; T is the temperature; and p is the pressure.

The Gibbs free energy for each phase is approximated within the quasi-harmonic approximation as $E_{\text{DFT}} + F_{\text{vib}} + pV$, where E_{DFT} is the DFT-calculated total energy at 0 K, F_{vib} is the vibrational free-energy contribution from phonon calculations and pV is the pressure–volume work term. The stable reference phases for the elements were chosen as follows: Li in a body-centred cubic structure (bcc, *Im*3*m*), Cu in a face-centred cubic structure (fcc, *Fm*3*m*), Sn in the β-Sn phase (*I*41/*amd*), Zn in a hexagonal close-packed structure (hcp, *P*63/*mmc*) and Se in a trigonal structure (*P*3121). The supercells of Cu_8Se_4, $Cu_8Sn_4Se_{12}$ and $Cu_8Zn_4Sn_4Se_{16}$ were used in the calculation. For Li alloying, one Li atom was introduced to substitute one Cu site in these supercells.

Device characterization

The m-TPC and modulated transient photovoltage (m-TPV) measurements were obtained by our lab-made set-up, in which the cell was excited by a tunable nanosecond laser pumped at 532 nm and recorded by a subnanosecond-resolved digital oscilloscope (Tektronix, DPO 7104) with a sampling resistance of 50 Ω or 1 MΩ. The current density–voltage (J–V) curves were recorded on a Keithley 2400 source meter under simulated air mass (AM) 1.5 sunlight at 100 mW cm^{-2}, calibrated with a Si reference cell (calibrated by the National Institute of Metrology (NIM) of China). The J–V test was conducted at 25 °C in air. The scanning speed was 90 mV s^{-1}. Each statistical box of device performance in Fig. 3a contains the data of 12 cells. The EQE was measured by an Enlitech QE-R test system using calibrated Si and Ge diodes as references. The drive-level capacitance profiling was measured on an electrochemical workstation (Versa STAT3, Princeton) by using 11 kHz and 100 kHz a.c. excitation with an amplitude from 10 to 100 mV and with a d.c. bias from 0 to −0.4 V. The thermal admittance spectroscopy test was also conducted on electrochemical workstation (Versa STAT3, Princeton).

Bending tests

Bending tests were conducted by using a flexible device to fit the curved surface of a wooden cylinder, which is described in detail in our previous work. The bending radius was determined by the size of the cylinder. In the bending radius test, all devices maintained a bending state for 10 s in each bending cycle. In the bending cycle testing, all devices maintained a bending state for 1 s in each bending cycle, with a bending radius of 20 mm.

Fabrication and stability evaluation of CZTSSe-shingled modules

CZTSSe-shingled modules were fabricated starting from a precursor film spin-coated on a 4.5 × 4 cm^2 molybdenum substrate. The film was patterned into 1.5 × 4 cm^2 strips by nanosecond laser scribing and subsequently selenized to form the CZTSSe absorber layer. A 50-nm-thick CdS buffer layer was deposited by chemical bath deposition, followed by sputtering of a 50 nm i-ZnO layer and a 250 nm ITO window layer. The top electrode, consisting of Ni (50 nm)/Al (3 µm) and a 110 nm anti-reflection layer, was then thermally evaporated.

To reduce edge recombination, the sub-cells were laser-cut from the back side, and the peripheral regions were mechanically removed, yielding effective cell areas of 1.3 × 3.7 cm^2. The sub-cells were connected in series using double-sided conductive adhesive tape to form a shingled module with electrical contacts at both ends, resulting in a CZTSSe-shingled module with an active area of 11.1 cm^2.

The device stability was evaluated through shelf-storage and light-soaking tests. For shelf stability, unencapsulated devices were stored in ambient air and periodically measured by *J*–*V* characterization. For operational stability, the device was continuously operated under ~1 sun light-emitting diode (LED) illumination with a 20 Ω load, and *J*–*V* curves were recorded at intervals to track performance degradation.

Reporting summary

Further information on research design is available in the Nature Portfolio Reporting Summary linked to this article.

Data availability

The main data supporting the findings of this study are available within the main text and Supplementary Information. Source data are provided with this paper.

References

1. Polman, A., Knight, M., Garnett, E. C., Ehrler, B. & Sinke, W. C. Photovoltaic materials: present efficiencies and future challenges. *Science* **352**, aad4424 (2016).
2. Gong, Y. et al. Elemental de-mixing-induced epitaxial kesterite/CdS interface enabling 13%-efficiency kesterite solar cells. *Nat. Energy* **7**, 966–977 (2022).
3. Feurer, T. et al. Progress in thin film CIGS photovoltaics – research and development, manufacturing, and applications. *Prog. Photovolt. Res. Appl.* **25**, 645–667 (2016).
4. Green, M. et al. Solar cell efficiency tables (version 66). *Prog. Photovolt. Res. Appl.* **33**, 795–810 (2025).
5. Xu, H. et al. Rapid grain growth to attain over 13% certified flexible CZTSSe solar cell. *ACS Energy Lett.* **10**, 4644–4654 (2025).
6. Lou, L. et al. Multi-interface engineering for all-solution-processed kesterite solar cells. *Joule* **9**, 9102091 (2025).
7. Li, J. et al. Emergence of flexible kesterite solar cells: progress and perspectives. *npj Flex. Electron.* **7**, 16 (2023).
8. Yang, K. J. et al. Sodium effects on the diffusion, phase, and defect characteristics of kesterite solar cells and flexible $Cu_2ZnSn(S,Se)_4$ with greater than 11% efficiency. *Adv. Funct. Mater.* **31**, 2102238 (2021).
9. López-Marino, S. et al. Alkali doping strategies for flexible and light-weight $Cu_2ZnSnSe_4$ solar cells. *J. Mater. Chem. A* **4**, 1895–1907 (2016).
10. Xu, X. et al. 12.84% efficiency flexible kesterite solar cells by heterojunction interface regulation. *Adv. Energy Mater.* **13**, 2301701 (2023).
11. Sutter-Fella, C. M. et al. Sodium assisted sintering of chalcogenides and its application to solution processed $Cu_2ZnSn(S,Se)_4$ thin film solar cells. *Chem. Mater.* **26**, 1420–1425 (2014).
12. Sangster, J. & Pelton, A. D. The Na-Se (sodium-selenium) system. *Phase Diagr. Eval. Sect. II* **18**, 185–189 (1997).
13. Cabas-Vidani, A. et al. High-efficiency $(Li_xCu_{1-x})_2ZnSn(S,Se)_4$ kesterite solar cells with lithium alloying. *Adv. Energy Mater.* **8**, 1801191 (2018).
14. Yuan, X. et al. Improved carrier collection efficiency in CZTS solar cells by Li-enhanced liquid-phase-assisted grain growth. *EcoEnergy* **2**, 181–191 (2024).
15. Zhao, K. et al. Li-based selenized Cu_2ZnSnS_4 surface: possible route to overcoming voc-deficit of kesterite solar cells. *Appl. Phys. Lett.* **118**, 252106 (2021).
16. Xin, H. et al. Lithium-doping inverts the nanoscale electric field at the grain boundaries in $Cu_2ZnSn(S,Se)_4$ and increases photovoltaic efficiency. *Phys. Chem. Chem. Phys.* **17**, 23859–23866 (2015).
17. Just, J. et al. Secondary phases and their influence on the composition of the kesterite phase in CZTS and CZTSe thin films. *Phys. Chem. Chem. Phys.* **18**, 15988–15994 (2016).
18. Dimitrievska, M. et al. Raman scattering quantitative analysis of the anion chemical composition in kesterite $Cu_2ZnSn(SxSe_{1-x})_4$ solid solutions. *J. Alloy. Compd.* **628**, 464–470 (2015).
19. Gong, Y. et al. Identifying the origin of the V_{oc} deficit of kesterite solar cells from the two grain growth mechanisms induced by Sn^{2+} and Sn^{4+} precursors in DMSO solution. *Energy Environ. Sci.* **14**, 2369–2380 (2021).
20. Yannopoulos, S. N. & Andrikopoulos, K. S. Raman scattering study on structural and dynamical features of noncrystalline selenium. *J. Chem. Phys.* **121**, 4747–4758 (2004).
21. Gong, X. et al. *In-situ* micro-Raman study of SnSe single crystals under atmosphere: effect of laser power and temperature. *Spectrochim. Acta A Mol. Biomol. Spectrosc.* **265**, 120375 (2022).
22. Xie, H. et al. Impact of Sn(S,Se) secondary phases in $Cu_2ZnSn(S,Se)_4$ solar cells: a chemical route for their selective removal and absorber surface passivation. *ACS Appl. Mater. Interfaces* **6**, 12744–12751 (2014).
23. Sava, F. et al. Amorphous $SnSe_2$ films. *J. Optoelectron. Adv. Mater.* **8**, 1367–1371 (2006).
24. Bernardini, G. P. & Catani, A. The Cu-Se system. *Miner. Deposita* **3**, 375–380 (1968).
25. Giraldo, S. et al. How small amounts of Ge modify the formation pathways and crystallization of kesterites. *Energy Environ. Sci.* **11**, 582–593 (2018).
26. Moser, S., Tiwari, A. N. & Carron, R. Interplay between Li and Na amid co-doped solution-processed $Cu_2ZnSn(S,Se)_4$ absorbers for solar cells. *Sol. Energy Mater. Sol. Cells* **250**, 112094 (2023).
27. Gokmen, T., Gunawan, O., Todorov, T. K. & Mitzi, D. B. Band tailing and efficiency limitation in kesterite solar cells. *Appl. Phys. Lett.* **103**, 014505 (2013).
28. Walter, T., Herberholz, R., Müller, C. & Schock, H. W. Determination of defect distributions from admittance measurements and application to $Cu(In,Ga)Se_2$ based heterojunctions. *J. Appl. Phys.* **80**, 4411–4420 (1996).
29. Azzouzi, M. et al. Analysis of the voltage losses in CZTSSe solar cells of varying Sn content. *J. Phys. Chem. Lett.* **10**, 2829–2835 (2019).
30. Jennifer, T. H., David, C. & William, N. S. Bulk and metastable defects in $CuIn_{1-x}Ga_xSe_2$ thin films using drive-level capacitance profiling. *J. Appl. Phys.* **95**, 1000–1010 (2004).
31. Larsen, J. K., Scragg, J. J. S., Ross, N. & Platzer-Björkman, C. Band tails and Cu–Zn disorder in Cu_2ZnSnS_4 solar cells. *ACS Appl. Energy Mater.* **3**, 7520–7526 (2020).
32. Wang, J. et al. Pd(II)/Pd(IV) redox shuttle to suppress vacancy defects at grain boundaries for efficient kesterite solar cells. *Nat. Commun.* **15**, 4344 (2024).
33. Yuan, Z. K. et al. Na-diffusion enhanced p-type conductivity in $Cu(In,Ga)Se_2$: a new mechanism for efficient doping in semiconductors. *Adv. Energy Mater.* **6**, 1601191 (2016).
34. Lu, Y.-N. et al. Constructing an n/n^+ homojunction in a monolithic perovskite film for boosting charge collection in inverted perovskite photovoltaics. *Energy Environ. Sci.* **14**, 4048–4058 (2021).
35. Li, Y. et al. Exploiting electrical transients to quantify charge loss in solar cells. *Joule* **4**, 472–489 (2020).
36. Shi, J., Li, D., Luo, Y., Wu, H. & Meng, Q. Opto-electro-modulated transient photovoltage and photocurrent system for investigation of charge transport and recombination in solar cells. *Rev. Sci. Instrum.* **87**, 123107 (2016).

37. Oh, W. et al. Metallization of crystalline silicon solar cells for shingled photovoltaic module application. *Sol. Energy* **195**, 527–535 (2020).
38. Hiroi, H., Sakai, N., Iwata, Y., Kato, T. & Sugimoto, H. Impact of buffer layer on kesterite solar cells. In *IEEE 42nd Photovoltaic Specialist Conference (PVSC)* https://doi.org/10.1109/PVSC.2015.7356415 (IEEE, 2015).
39. Yin, X., Tang, C., Sun, L., Shen, Z. & Gong, H. Study on phase formation mechanism of non- and near-stoichiometric $Cu_2ZnSn(S,Se)_4$ film prepared by selenization of Cu–Sn–Zn–S precursors. *Chem. Mater.* **26**, 2005–2014 (2014).
40. Xie, W. et al. 10.24% efficiency of flexible $Cu_2ZnSn(S,Se)_4$ solar cells by pre-evaporation selenization technique. *Small* **18**, 2201347 (2022).
41. Yan, Q. et al. Enhancing carrier transport in flexible CZTSSe solar cells via doping Li strategy. *J. Energy Chem.* **75**, 8–15 (2022).
42. Son, D. H. et al. Vertical plane depth-resolved surface potential and carrier separation characteristics in flexible CZTSSe solar cells with over 12% efficiency. *Carbon Energy* **6**, e434 (2024).
43. Sun, Q. et al. Defect synergistic regulations of Li & Na co-doped flexible $Cu_2ZnSn(S,Se)_4$ solar cells achieving over 10% certified efficiency. *Adv. Sci.* **11**, e2306740 (2024).
44. Ahn, K. et al. Flexible high-efficiency CZTSSe solar cells on stainless steel substrates. *J. Mater. Chem. A* **7**, 24891–24899 (2019).
45. Xu, H. et al. 9.63% efficient flexible $Cu_2ZnSn(S,Se)_4$ solar cells fabricated via scalable doctor-blading under ambient conditions. *J. Mater. Chem. A* **9**, 25062–25072 (2021).
46. Deng, H. et al. Novel symmetrical bifacial flexible CZTSSe thin film solar cells for indoor photovoltaic applications. *Nat. Commun.* **12**, 3107 (2021).
47. Jeong, W. L. et al. Impact of Na doping on the carrier transport path in polycrystalline flexible $Cu_2ZnSn(S,Se)_4$ solar cells. *Adv. Sci.* **7**, 1903085 (2020).
48. Liu, S. et al. Dual-functional GeSe–Se coselenization enabling synergistic defect-interface engineering for high-efficiency electrodeposited flexible CZTSe solar cells. *Nano Lett.* **25**, 13144–13152 (2025).
49. Gobbo, C. et al. Strategies for back contact engineering in high-performance flexible kesterite solar cells. *J. Mater. Chem. A* **13**, 25498–25508 (2025).
50. Xu, H. et al. 11.88% efficient flexible Ag-free CZTSSe solar cell: spontaneously tailoring the alkali metal level. *Small* **20**, e2408122 (2024).
51. Su, Z. et al. Overcoming back interfacial barrier improves flexible $Cu_2ZnSn(S,Se)_4$ solar cell efficiency via CuO sacrificial layers. *ACS Mater. Lett.* **7**, 1329–1335 (2025).
52. Ji, Y. et al. A quasi-ohmic back contact achieved by inserting single-crystal graphene in flexible kesterite solar cells. Preprint at https://arxiv.org/abs/2408.15684 (2024).
53. Zhang, Y. et al. Flexible CZTSSe solar cells with 11.21% efficiency enabled by O-doped CZTSSe/CdS heterojunction. *J. Energy Chem.* **105**, 806–813 (2025).
54. Yang, K. J. et al. Flexible $Cu_2ZnSn(S,Se)_4$ solar cells with over 10% efficiency and methods of enlarging the cell area. *Nat. Commun.* **10**, 2959 (2019).
55. Antunez, P. D., Bishop, D. M., Luo, Y. & Haight, R. Efficient kesterite solar cells with high open-circuit voltage for applications in powering distributed devices. *Nat. Energy* **2**, 884–890 (2017).
56. Larramona, G. et al. Stability, reliability, upscaling and possible technological applications of kesterite solar cells. *J. Phys. Energy* **2**, 024009 (2020).
57. Hiroi, H., Sakai, N. & Sugimoto, H. Development of high efficiency Cu_2ZnSnS_4 solar cells and modules. In *Proc. 26th European Photovoltaic Solar Energy Conference* https://doi.org/10.4229/26thEUPVSEC2011-3DO.8.2 (2011).
58. Hiroi, H., Sakai, N. & Sugimoto, H. Cd-free 5×5cm^2-sized Cu2ZnSnS4 submodules. In *37th IEEE Photovoltaic Specialists Conference* https://doi.org/10.1109/PVSC.2011.6186509 (IEEE, 2011).
59. Sugimoto, H., Hiroi, H., Sakai, N., Satoshi, M. & Takuya, K. Over 8% efficiency Cu2ZnSnS4 submodules with ultra-thin absorber. In *38th IEEE Photovoltaic Specialists Conference* https://doi.org/10.1109/PVSC.2012.6318214 (IEEE, 2012).
60. Kato, T., Hiroi, H., Sakai, N. & Sugimoto, H. Buffer/absorber interface study on Cu_2ZnSnS_4 and $Cu_2ZnSnSe_4$-based solar cells: band alignment and its impact on the solar cell performance. In *28th European Photovoltaic Solar Energy Conference* https://doi.org/10.4229/28thEUPVSEC2013-3AO.5.1 (2013).
61. Yuan, M. et al. 4.3% efficient kesterite solar cell modules. *Sci. Bull.* **68**, 1497–1499 (2023).
62. Xiang, C. et al. Solution-processed kesterite solar module with 10.1% certified efficiency. *Nat. Energy* https://doi.org/10.1038/s41560-025-01860-3 (2025).
63. Wang, W. et al. Device characteristics of CZTSSe thin-film solar cells with 12.6% efficiency. *Adv. Energy Mater.* **4**, 1301465 (2014).
64. Kim, J. et al. High efficiency $Cu_2ZnSn(S,Se)_4$ solar cells by applying a double In_2S_3/CdS emitter. *Adv. Mater.* **26**, 7427–7431 (2014).

Acknowledgements

This work was supported by the National Key R&D Program of China (2024YFB4205000 to J.S.); the National Natural Science Foundation of China (52222212 to J.S., 52227803 to Q.M., 52172261 to Y. Luo, 52402243 to X.X. and 52502322 to Jinlin Wang); the Zhejiang Provincial Natural Science Foundation (LQN25E020011 to X.X.); and the China National Postdoctoral Program for Innovative Talents (BX20250177 to Jinlin Wang). J.S. also gratefully acknowledges support from the Youth Innovation Promotion Association of the Chinese Academy of Sciences (2022006).

Author contributions

The manuscript was written through the contribution of all authors. All authors have given approval for the final version of the manuscript. Q.M., J.S. and W.Y. contributed to the supervision, discussion and writing (review and editing). X.X. and Jinlin Wang contributed to the experiments, simulation, characterization and writing (original draft). H.W. contributed to the discussion. M.J., B.Z., T.G., Yuan Li, Jinchen Wang and S.C. contributed to the data analysis and discussion. J.S. and Yiming Li contributed to the discussion and m-TPC/m-TPV analyses. D.L. and Y. Luo contributed to the data analysis.

Competing interests

The authors declare no competing interests.

Additional information

Supplementary information The online version contains supplementary material available at https://doi.org/10.1038/s41560-026-02018-5.

Correspondence and requests for materials should be addressed to Jiangjian Shi, Wensheng Yan or Qingbo Meng.

Peer review information *Nature Energy* thanks Victor Izquierdo-Roca and the other, anonymous, reviewer(s) for their contribution to the peer review of this work.

nature portfolio

Corresponding author(s): Qingbo Meng, Jiangjian shi, Wenshen yan

Solar Cells Reporting Summary

Nature Portfolio wishes to improve the reproducibility of the work that we publish. This form is intended for publication with all accepted papers reporting the characterization of photovoltaic devices and provides structure for consistency and transparency in reporting. Some list items might not apply to an individual manuscript, but all fields must be completed for clarity.

For further information on Nature Research policies, including our data availability policy, see Authors & Referees.

Experimental design

Please check the following details are reported in the manuscript, and provide a brief description or explanation where applicable.

1. Dimensions

Area of the tested solar cells	☒ Yes ☐ No	The area of the small-area device is 0.2296 cm2,and that of the minimodule is 10.47 cm2. *Explain why this information is not reported/not relevant.*
Method used to determine the device area	☒ Yes ☐ No	These two areas were determined by defining the illuminated area using two calibrated shadow masks. *Explain why this information is not reported/not relevant.*

2. Current-voltage characterization

Current density-voltage (J-V) plots in both forward and backward direction	☒ Yes ☐ No	Both forward and reverse scans are provided in the certification report, and the cells exhibited no hysteresis.
Voltage scan conditions	☒ Yes ☐ No	The voltage scan range was from –50 mV to 600 mV and its scanning speed is 90 mV s-1. *Explain why this information is not reported/not relevant.*
Test environment	☒ Yes ☐ No	The measurements were conducted in an ambient atmosphere at approximately 25 ° C. *Explain why this information is not reported/not relevant.*
Protocol for preconditioning of the device before its characterization	☐ Yes ☒ No	*Provide a description of the protocol.* No special treatment was required for the cells prior to testing.
Stability of the J-V characteristic	☐ Yes ☒ No	*Provide a description of the method used. The stability of the J-V characteristic can be verified with time evolution of the maximum power point or with the photocurrent at maximum power point; see ref. 5 for details.* The steady-state output of CZTSSe solar cells is stable and shows no issues.

3. Hysteresis or any other unusual behaviour

Description of the unusual behaviour observed during the characterization	☐ Yes ☒ No	*Provide a description of hysteresis or any other unusual behaviour observed during the characterization.* No abnormal conditions occurred during the testing process.
Related experimental data	☐ Yes ☒ No	*Provide a description of the related experimental data.* No abnormal conditions occurred during the testing process.

4. Efficiency

External quantum efficiency (EQE) or incident photons to current efficiency (IPCE)	☒ Yes ☐ No	External quantum efficiency was measured by Enlitech QE-R test system using calibrated Si and Ge diodes as references. *Explain why this information is not reported/not relevant.*
A comparison between the integrated response under the standard reference spectrum and the response measure under the simulator	☒ Yes ☐ No	EQE spectrum and the corresponding integrated current density of the cell are shown in Figure 3, which agrees well with the I–V measurement results. *Explain why this information is not reported/not relevant.*

For tandem solar cells, the bias illumination and bias voltage used for each subcell

☐ Yes
☒ No

Provide a description of the measurement conditions.

This work does not involve tandem devices.

5. Calibration

Light source and reference cell or sensor used for the characterization

☒ Yes
☐ No

AM 1.5 sunlight at 100 mW cm^{-2} was used, calibrated with a Si reference cell (calibrated by NIM).

Explain why this information is not reported/not relevant.

Confirmation that the reference cell was calibrated and certified

☒ Yes
☐ No

Si reference cell is calibrated by NIM.

Explain why this information is not reported/not relevant.

Calculation of spectral mismatch between the reference cell and the devices under test

☒ Yes
☐ No

The mismatch factors are provided in Figures S22 and S28 of the Supporting Information, being 1.014 for the small-area cell and 1.016 for the minimodule.

Explain why this information is not reported/not relevant.

6. Mask/aperture

Size of the mask/aperture used during testing

☒ Yes
☐ No

The mask areas were 0.2296 cm^2 for the small-area device and 10.47 cm^2 for the minimodule.

Explain why this information is not reported/not relevant.

Variation of the measured short-circuit current density with the mask/aperture area

☐ Yes
☒ No

Report the difference in the short-circuit current density values measured with the mask and aperture area.

To ensure the accuracy of all current measurements, all devices were tested under the corresponding shadow masks.

7. Performance certification

Identity of the independent certification laboratory that confirmed the photovoltaic performance

☒ Yes
☐ No

Both certification are conducted by National PV Industry Measurement and Testing Center.

Explain why this information is not reported/not relevant.

A copy of any certificate(s)

☒ Yes
☐ No

The certificates are provided in Figures S22 and S28, respectively.

Explain why this information is not reported/not relevant.

8. Statistics

Number of solar cells tested

☒ Yes
☐ No

12 cells for each condition.

Explain why this information is not reported/not relevant.

Statistical analysis of the device performance

☒ Yes
☐ No

The statistical analysis data are presented in Figures 1b-c, 3a-b, S12, S14, S15, S21

Explain why this information is not reported/not relevant.

9. Long-term stability analysis

Type of analysis, bias conditions and environmental conditions

☒ Yes
☐ No

For shelf stability, unencapsulated devices were stored in ambient air and periodically measured by J–V characterization with initial PCE of 11.7%. For operational stability, the device (initial PCE 11.3%) was continuously illuminated (white LED, ~ 1 sun intensity) with a load of ~20 Ω in ambient temperature and atmosphere conditions. The ambient temperature is about 25 °C and no temperature control of the device was used. The device efficiency at different sampling points was measured under standard conditions using simulated AM 1.5G light.

Explain why this information is not reported/not relevant.